Optik - International Journal for Light and Electron Optics 290 (2023) 171312

Contents lists available at ScienceDirect

Optik

journal homepage: www.elsevier.com/locate/ijleo

A highly sensitive six-conjoined-tube anti-resonance optical fiber temperature sensor based on surface plasmon resonance

Haihao Fu [a], Shuqin Lou [a,*], Wei Gao [a], Donglian Hou [a], Paul K. Chu [b]

[a] School of Electronic Information Engineering, Beijing Jiaotong University, Beijing 100080, PR China
[b] Department of Physics, Department of Materials Science and Engineering, and Department of Biomedical Engineering, City University of Hong Kong, Tat Chee Avenue, Kowloon, Hong Kong, China

ARTICLE INFO

Keywords:
Surface plasmon resonance
Anti-resonant fiber
Optical fiber sensing
Sensitivity

ABSTRACT

Object: Owing to advances in optical fiber sensing, sensing techniques based on surface plasmon resonance (SPR) have received much attention. In this work, an SPR temperature sensor based on the anti-resonant fiber (ARF) is designed and analyzed. By filling the core with a thermosensitive liquid, the ambient temperature in the range of 5–55 °C can be detected.
Methods: The proposed ARF was simulated utilizing the finite element analysis software COMSOL, followed by systematic and comprehensive structural parameter optimization, and the basic characteristics of the ARF-SPR temperature sensor were analyzed. Filling with a gold medium instead of the traditional coating process reduces the difficulty in manufacturing the ARF-SPR temperature sensor.
Results: The average temperature sensitivity of the ARF-SPR sensor is 16.055 nm/°C, the minimum structural parameter sensitivity is 1.0 nm/μm, and the maximum FOM is 360.8 $°C^{-1}$ at 5 °C. The ARF sensor with excellent properties has large commercial potential in biochemical analysis, temperature monitoring, as well as long-distance sensing.

1. Introduction

An optical sensor is a device that uses an optical signal to detect regular changes in some physical entities of an analyte under external stimulation [1]. The common optical sensors are the F-P interference air bubble microcavity sensors [2], Bragg grating sensors [3], and optical fiber sensors [4–6]. In recent years, optical fiber sensing technology has received great attention due to advantages such as strong anti-electromagnetic interference ability, low loss, no marking, and real-time monitoring.

The beam from a specific light source is totally reflected after entering the optical fiber sensor [7]. Owing to the changes in physical quantities such as the refractive index, strain, magnetic field, and temperature of the detection environment, the wavelength, phase, frequency, and polarization of incident light change regularly according to a certain corresponding relationship [8]. The modulated optical signal is converted into the electrical signal by the demodulator and then output for measurement, thus accomplishing optical fiber sensing. In order to detect the modulated light signal more efficiently, it is necessary to seek a feasible method to alter some characteristics of light. Surface plasmon resonance (SPR) is a physical optical phenomenon widely adopted in optical fiber sensing [9]. When the incident light with a certain frequency impinges onto a metal surface, it will be coupled with the surface plasma wave (SPW) on the materials, and the energy will be transferred from photons to the surface plasmons, resulting in changes in some characteristics

* Corresponding author.
E-mail address: shqlou@bjtu.edu.cn (S. Lou).

https://doi.org/10.1016/j.ijleo.2023.171312
Received 1 July 2023; Received in revised form 10 August 2023; Accepted 15 August 2023
Available online 18 August 2023

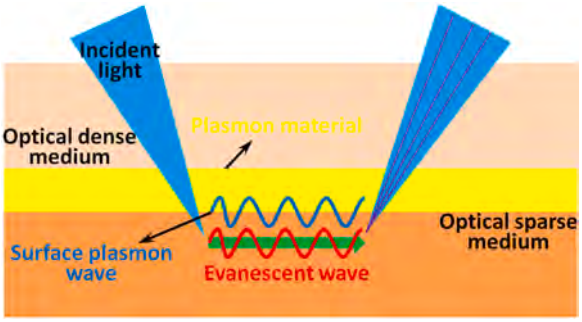

Fig. 1. Principle of the SPR phenomenon.

of the incident light [10].

Many optical fibers can be used for SPR sensing, for example, the single mode fiber (SMF) [11], photonic crystal fiber (PCF) [12–14], and SPR fiber sensors [15–18]. In 2020, X. Guo et al. [19] have designed a D-shape polished dual-core PCF refractive index sensor based on SPR, which can detect analytes with refractive indexes in the range of 1.33–1.43. Liu et al. [20] have proposed a photonic quasi-crystal fiber (PQF) sensor using the $OAM_{1,1}$ mode to excite SPR for the refractive index range of 1.36–1.435. Most of the SPR sensors are based on PCF, and there have been few studies on anti-resonant fiber (ARF) SPR sensors. ARF is a microstructure composed of negative curvature anti-resonant tubes. When the light is transmitted to the interface between the core and cladding, the light meeting the anti-resonance conditions will be directly propagated from the cladding, while other that does not dissatisfy the conditions will be reflected back to the core [21]. ARF not only has a simpler structure, but also exhibits a lower loss due to its special light transmission principle. J. Lv et al. [22] have designed an SPR refractive index sensor based on ARF with an amplitude sensitivity of 2573.33 RIU^{-1}. If a thermosensitive liquid fills the core of ARF, the effective refractive index of the fundamental mode will change correspondingly at different temperatures, and the ARF-SPR temperature sensor can be designed. Q. Wang et al. [23] have proposed an eight-conjoined tube ARF-SPR temperature sensor with more than 6 resonance peaks in different bands. Q. Chen et al. [24] have designed a hollow-core negative curvature ARF with a maximum temperature sensitivity is 5.047 nm/°C. However, the sensitivity of these temperature sensors is still low and further development is necessary.

Herein, a six-conjoined-tube ARF temperature sensor based on SPR is designed and the structural parameters are optimized to achieve the best temperature sensing properties. The structural parameters investigated include the diameter of the guide mode, the thickness of the negative curvature tube, the composition ratio of the thermosensitive liquid, and the inner diameters of the inner and outer negative curvature tubes. The mode field distribution, temperature sensing, and amplitude sensitivity of the ARF-SPR sensor are derived by the finite element method (FEM) [25,26]. The numerical results indicate that the ARF-SPR sensor can detect temperatures in the range of 5–55 °C with a maximum temperature sensitivity of 19.4 nm/°C. The longest detection distance and highest FOM are 20.17 m and 360.8 $°C^{-1}$ respectively, suggesting great commercial potential in environmental monitoring and chemical analysis.

2. ARF design and sensing principle

When a light beam is emitted from a light dense medium to a light sparse medium, total reflection will occur under certain conditions. If the incident light reaches the interface of the two media, the reflected light will not be generated immediately. Instead, it will first pass through the light sparse medium about a depth of about one wavelength and propagate along the axial direction for half a wavelength before returning to the optically dense medium. The wave flowing along the axial direction is called an evanescent wave, and its propagation constant is shown in Eq. (1) [27]:

$$K = \frac{\omega}{c}\sqrt{\varepsilon_1(\omega)}\sin\theta_i, \tag{1}$$

where ω is the frequency of the incident light, ε_1 is the dielectric constant of the optically dense medium at this frequency, c is the speed of light, and θ_i is the incident angle of the light wave. When a definite frequency of incident light reaches the metal surface, it will disrupt the uniform distribution of electron density. If the regional electron density is a smaller amount than the average electron density, positively charged particles cannot be completely neutralized. To maintain electrical neutrality, a large number of electrons are attracted to this region. When the number of electrons is sufficient, the repulsion between them is greater than the attraction of a positive charge to them, and the electrons will be driven away. The cyclic motion of electrons on a metal surface is called plasma oscillation, and the resulting charge density wave is called SPW. The propagation constant of SPW can be obtained by Eq. (2) [28]:

$$K_{spw} = \frac{\omega}{c}\sqrt{\frac{\varepsilon_m(\omega)\varepsilon_2}{\varepsilon_m(\omega)+\varepsilon_2}}, \tag{2}$$

where $\varepsilon_m(\omega)$ and ε_2 are the dielectric constants of the metal and optically sparse medium, respectively, and ω is the frequency of the incident light. When $\boldsymbol{K} = \boldsymbol{k_{spw}}$, the evanescent wave resonates with the SPW, and the reflected light intensity decreases greatly. The

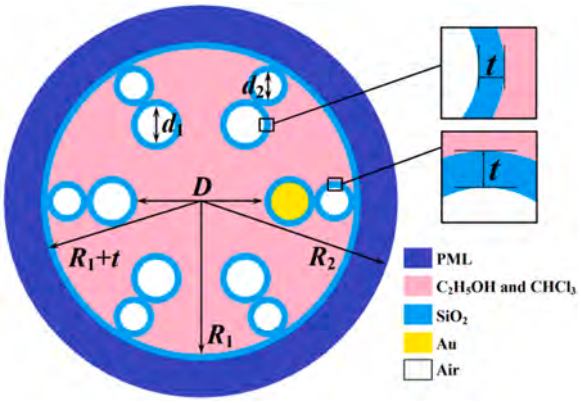

Fig. 2. Cross-section of the ARF-SPR sensor.

incident angle corresponding to the lowest intensity is defined as the resonance angle. Because SPR is very sensitive to the refractive index of the medium attached to the metal surface, the resonance angle will change with different environmental physical entities. The principle is illustrated in Fig. 1.

In the ARF-SPR sensor, the negative curvature anti-resonance tube is a light dense medium and the thermosensitive liquid is a light sparse medium. SPR is essentially the energy exchange between the guided mode and the metal surface plasmon (SPP), which can be characterized by the confinement loss of the guided mode in a certain band. The loss can be computed by Eq. (3) [29], and the wavelength corresponding to the loss peak is called the resonance wavelength:

$$L = \frac{2\pi}{\lambda}\frac{20}{\ln(10)}10^4 \mathrm{Im}\left(n_{eff}\right) \Big/ \left(dB/cm\right), \tag{3}$$

where λ is the wavelength, $\mathrm{Im}(n_{eff})$ is the imaginary part of the effective refractive index. The ARF-SPR temperature sensing structure is described in Fig. 2.

The ARF-SPR sensor consists of six groups of conjoined anti-resonance tubes. Each group is composed of two negative curvature tubes with inner diameters of $\boldsymbol{d_1}$ and $\boldsymbol{d_2}$, respectively. Six groups of conjoined tubes are placed in a large glass tube with an inner radius of $\boldsymbol{R_1}$ and are tangent to the large glass tube to form a guided mode region with a diameter of $\boldsymbol{D}$. The conjoined tube and large glass tube with identical thickness $\boldsymbol{t}$ are both made of SiO_2. The thickness of the negative curvature tube should satisfy the anti-resonance condition given in formula (4) [22]:

$$t = \frac{\lambda m}{2\sqrt{n_1^2 - n_0^2}}, \tag{4}$$

where λ is the wavelength, m is the order of resonance generally equal to 1 to obtain a large anti-resonance region, and n_1 and n_0 are the refractive indexes of SiO_2 and core. Since the sensor is designed to detect temperature, the influence of temperature must be considered when calculating the refractive index of SiO_2. The formula is expressed in (5) [30]:

$$n^2\left(\lambda, T\right) = 1.31552 + A_1 T + \frac{\left(B_1 + B_2 T\right)\lambda^2}{\lambda^2 - \left(B_3 + B_4 T\right)} + \frac{\left(C_1 + C_2 T\right)\lambda^2}{\lambda^2 - 100}, \tag{5}$$

where $A_1 = 6.90754 \times 10^{-6}$, $B_1 = 0.788404$, $B_2 = 2.35835 \times 10^{-5}$, $B_3 = 0.0110199$, $B_4 = 0.584758 \times 10^{-6}$, $C_1 = 0.91316$, $C_2 = 0.548368 \times 10^{-6}$, λ is the wavelength, and T is the ambient temperature. The pink area is the thermosensitive liquid for temperature sensing, which is mixed with a certain amount of ethanol and chloroform. The reason why chloroform is selected as the thermosensitive liquid is that the thermo-optic coefficient is large, but its refractive index is high, and a certain amount of ethanol needs to be added to reduce the refractive index. The refractive index of the thermosensitive liquid is a function of temperature is determined by Eq. (6) [24]:

$$n_{mix} = A\left[n_{eth}|_{T=T_0} + \frac{dn_{eth}}{dT}\left(T - 20\right)\right] + \left(1 - A\right)\left[n_{chl}|_{T=T_0} + \frac{dn_{chl}}{dT}\left(T - 20\right)\right], \tag{6}$$

where A and (1-A) are the concentrations of C_2H_5OH and $CHCl_3$ respectively, and $n_{eth}|_{T=T0}$ and $n_{chl}|_{T=T0}$ are the refractive indexes of ethanol and chloroform at 20 °C as shown by Eq. (7) [31] and (8) [31]:

$$n_{eth}^2|_{T=T_0} = 1 + \frac{0.83189\lambda^2}{\lambda^2 - 0.00930} - \frac{0.15582\lambda^2}{\lambda^2 + 49.4520}, \tag{7}$$

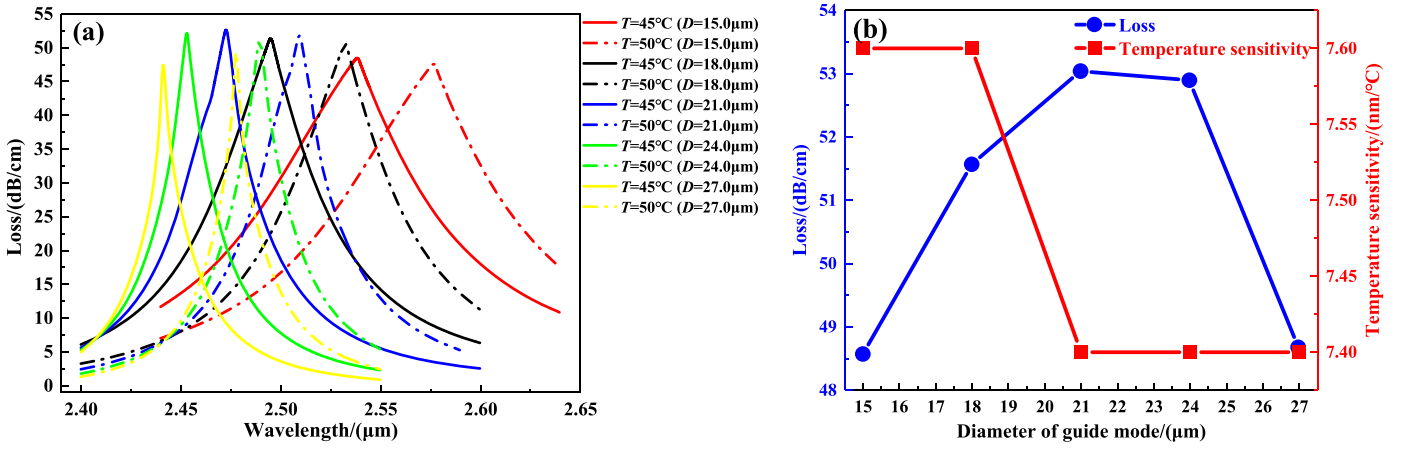

Fig. 3. (a) Optimization of the diameter of the guide mode and (b) Result summary.

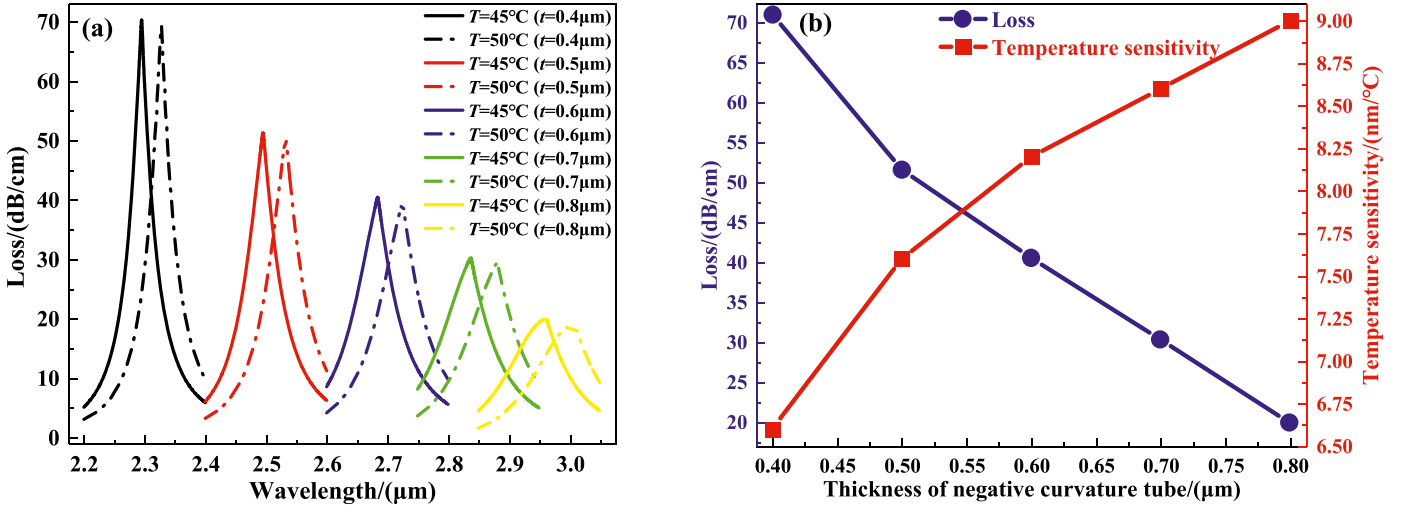

Fig. 4. (a) Optimization of the thickness of the negative curvature tubes and (b) Result summary.

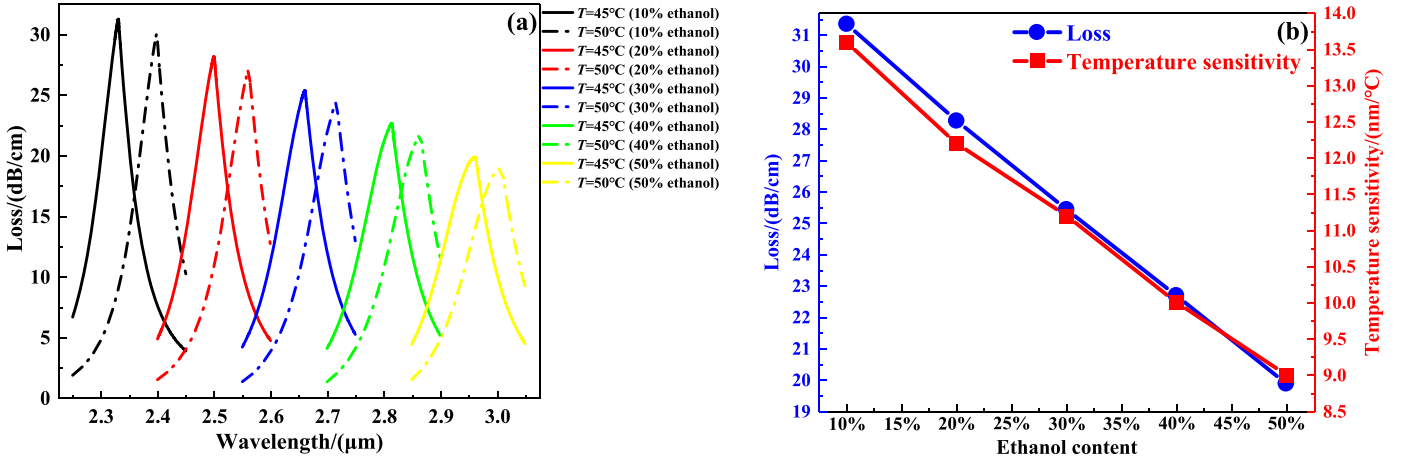

Fig. 5. (a) Optimization of the ethanol concentration in the thermosensitive liquid and (b) Result summary.

$$n_{chl}^2\big|_{T=T_0} = 1 + \frac{1.04647\lambda^2}{\lambda^2 - 0.01048} + \frac{0.00345\lambda^2}{\lambda^2 - 0.15207}, \tag{8}$$

where $dn_{eth}/dT = -3.94 \times 10^{-4}$ /°C and $dn_{chl}/dT = -6.328 \times 10^{-4}$ /°C are the thermo-optic coefficients of C_2H_5OH and $CHCl_3$, respectively. Since the boiling points of ethanol and chloroform are 78.4 °C and 61.3 °C respectively, the highest temperature that can be detected by the mixed thermosensitive liquid with the two substances is 60 °C. In addition, one of the negative curvature tubes is filled with an Au medium as the plasmonic material, which effectively reduces the difficulty in preparation compared to the traditional coating process. The relative dielectric constant of Au can be calculated by Eq. (9) [32]:

$$\varepsilon_{Au}(\omega) = \varepsilon_\infty - \frac{\omega_p^2}{\omega(\omega + i\omega_\tau)}, \tag{9}$$

where $\varepsilon_\infty = 9.75$, $\omega_p = 1.36 \times 10^{16}$ rad/s, and $\omega_\tau = 1.45 \times 10^{14}$ rad/s. In fact, the plasma frequency ω_p undergoes slight changes in high-temperature environments. However, within the detection range of 5–55 °C, the fluctuation of ω_p is not significant [17], and the impact on the dielectric constant and refractive index of Au is even negligible. In addition, when the variation in temperature is identical, the change in refractive index of thermosensitive liquid is much higher than gold. Therefore, for the proposed ARF-SPR sensor, the temperature characteristic of the gold dielectric constant can be ignored. The dark blue region of the outermost layer of the fiber with a radius of $\boldsymbol{R_2}$ is the perfect matching layer (PML) that can absorb all the electromagnetic waves and provides the ideal boundary condition.

The structural parameters of the optical fiber and the composition of the thermosensitive liquid have significant effects on the performance of the ARF-SPR temperature sensor thus requiring optimization. Based on the temperature sensitivity of the ARF-SPR sensor at 45 °C expressed in Eq. (9) [33], the diameter $\boldsymbol{D}$ of the guide mode, the thickness $\boldsymbol{t}$ of the negative curvature tube, the amount of ethanol in the thermosensitive liquid, and the inner diameter $\boldsymbol{d_1}$ and $\boldsymbol{d_2}$ of the inner and outer tube are optimized:

$$S_n = \frac{\Delta\lambda_{peak}}{\Delta T}, \tag{10}$$

where $\triangle\lambda_{peak}$ is the resonance wavelength difference at adjacent temperatures and $\triangle T$ is the temperature difference. The reason why temperature sensitivity as a benchmark for optimization is that S_n not only directly determines the detection accuracy of the proposed ARF-SPR sensor, but has a more significant change in temperature sensitivity compared to other performance under different structural parameters, which is more conducive to performance optimization. In addition, $\boldsymbol{D}$, $\boldsymbol{t}$, and the ethanol content are more sensitive to S_n compared with $\boldsymbol{d_1}$ and $\boldsymbol{d_2}$, therefore it is more reasonable in this order for optimizing. The initial parameters of the sensor are: $\boldsymbol{D} = 15.0$ μm and $\boldsymbol{t} = 0.5$ μm, the concentration of C_2H_5OH is 50 %, $\boldsymbol{d_1} = 4.8$ μm, and $\boldsymbol{d_2} = 4.0$ μm.

Based on these original parameters, we first optimize the diameter of the guide mode. When the guide mode diameter is less than 14.88 μm, the loss of the core fundamental mode is proportional to the wavelength at all times, and the loss peak does not exist. On the other hand, when it is greater than 27.21 μm, the optical wave cannot be completely limited in the core, and a large number of photons leak into the outer layer, resulting in distortion of the fundamental mode. Therefore, $\boldsymbol{D}$ is optimized within 15–27 μm, and the specific process is displayed in Fig. 3(a) and (b).

With increasing wavelength, the loss at any temperature and diameter increases first and then decreases, and the perfect resonance peak exists. When $\boldsymbol{D}$ increases, the resonance wavelength blueshifts, and the temperature sensitivity abates. When the diameter of the guide mode is 15 μm or 18 μm, the temperature sensitivity is 7.6 nm/°C. Here, the reason why the $\boldsymbol{D}$ is set as 18 μm is that the resonance is stronger for this diameter.

After the guide mode diameter is determined, we optimize the thickness of the negative curvature tube. When $\boldsymbol{t} < 0.395$ μm, the loss of the fundamental mode is too high, and according to the anti-resonance condition given in Eq. (4), the minimum $\boldsymbol{t}$ value affecting SPR is 0.823 μm. Therefore, the pipe wall thickness is optimized in the range of 0.4–0.8 μm as shown in Fig. 4(a) and (b).

Fig. 4 indicates that the thickness of the negative curvature tubes of the ARF-SPR sensor has a significant impact on the temperature sensing performance. For the same thickness, the resonance wavelength is positively correlated with the temperature, and the temperature sensitivity is directly proportional to the thickness of the negative curvature tube. In addition, with increasing $\boldsymbol{t}$, the resonance wavelength redshifts, and the loss of the fundamental mode also decreases. When $\boldsymbol{t} = 0.8$ μm, the temperature sensitivity is 9.0 nm/°C, which is the highest in the set optimization range. Consequently, the thickness of the negative curvature tube is selected to be 0.8 μm.

The amount of ethanol and chloroform in the thermosensitive liquid is an important factor affecting the performance of ARF-SPR. The reason why we choose to optimize in the range of ethanol concentration of 10–50 % (chloroform concentration of 90–50 %) is that if the ethanol concentration is less than 10 %, the refractive index of chloroform cannot be reduced, but at above 50 %, there is no effective resonance peak. As shown in Fig. 5(a) and (b), with a reduced amount of ethanol, the resonance wavelength at both temperatures shifts to the short wavelength direction, and the resonance intensity also increases, which is more conducive to exciting SPR. When the ratio of C_2H_5OH to $CHCl_3$ is 1:9, the temperature sensitivity shows a maximum value in the optimized range, which is 13.6 nm/°C. Therefore, the ethanol concentration should be 10 % and chloroform is 90 % in preparing the thermosensitive liquid.

Based on $\boldsymbol{D} = 18.0$ μm and $\boldsymbol{t} = 0\ 8$ μm, C_2H_5OH: $CHCl_3 = 1$: 9, we optimize the inner diameter of the inner negative curvature tube. When $\boldsymbol{d_1} < 2.97$ μm, the fundamental mode photon energy cannot be well bound in the core, resulting in mode distortion. When the diameter is greater than 5.45 μm, the electric field direction of the fundamental mode will deviate. Therefore, the appropriate $\boldsymbol{d_1}$ is in the range of 3–5.4 μm as shown in Fig. 6(a) and (b).

As the inner diameter of the inner tube increases, the resonance wavelength redshifts, and the resonance wavelength difference

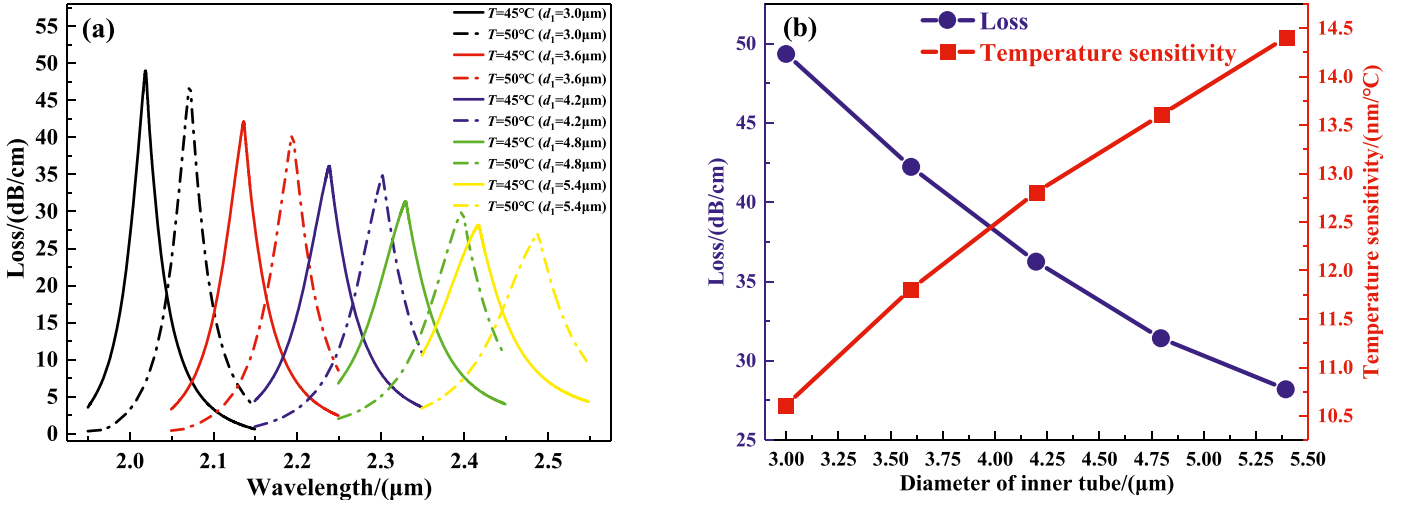

Fig. 6. (a) Optimization of d_1 in the range of 3.0–5.4 μm and (b) Summary of relevant results.

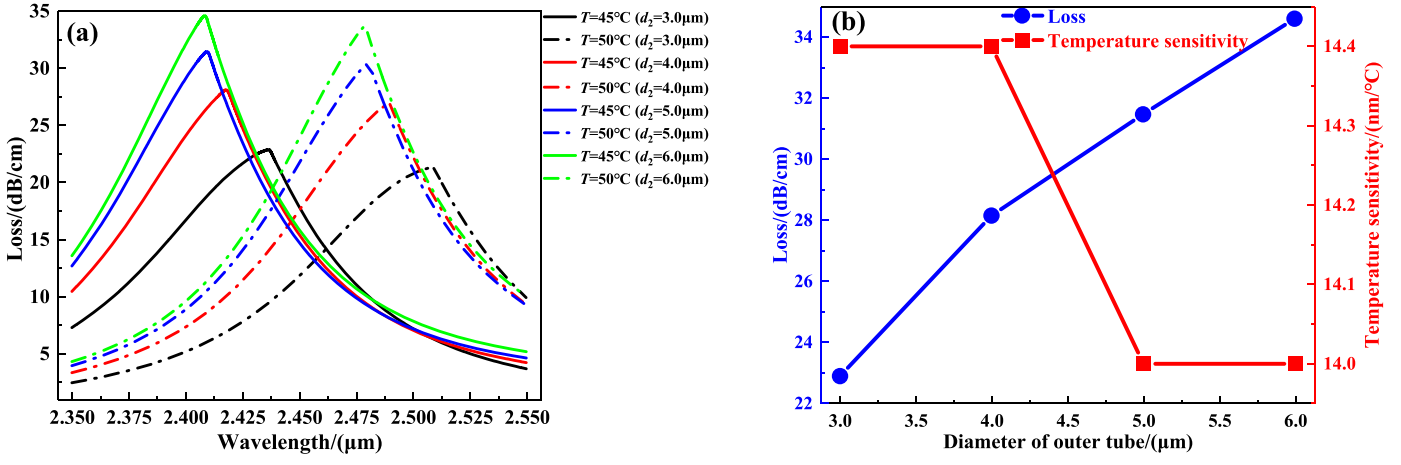

Fig. 7. (a) Optimization of d_2 in the range of 3.0–6.0 μm and (b) Summary of relevant results.

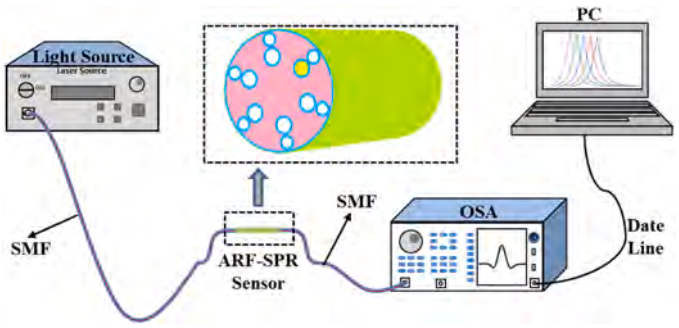

Fig. 8. Schematic showing the detection of temperature by the ARF-SPR sensor.

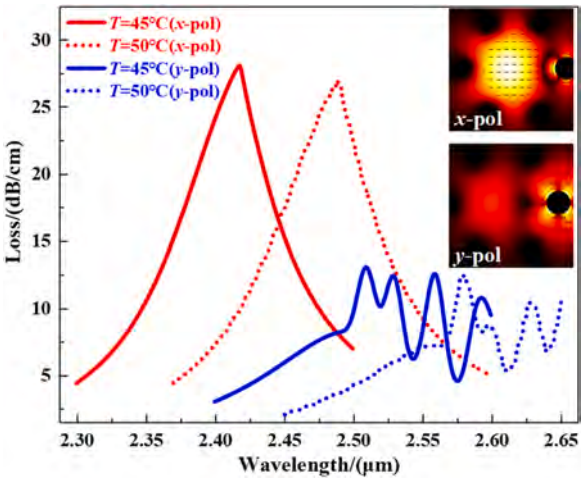

Fig. 9. Loss spectra and mode field distributions of the two polarizations at 45 °C and 50 °C.

corresponding to the adjacent temperature also goes up. In addition, the loss at 45 °C is inversely proportional to $\boldsymbol{d_1}$ and directly proportional to the temperature sensitivity. The maximum temperature sensitivity (14.4 nm/°C) is achieved when the inner diameter of the inner tube is 5.4 μm. Therefore, $\boldsymbol{d_1}$ is set at 5.4 μm.

Finally, we optimize the inner diameter of the outer negative curvature tube. In fact, setting the outer tube is to further limit the light wave to the core. Compared to other structural parameters, $\boldsymbol{d_2}$ is less susceptible to temperature, but it still needs to be optimized. When $\boldsymbol{d_2}$ is less than 2.94 μm, the core energy will leak. When $\boldsymbol{d_2} > 6.02$ μm, the imaginary part of the fundamental mode refractive index is negative, leading to loss without physical significance. Therefore, the optimal inner diameter of the outer tube is between 3 μm and 6 μm. As shown in Fig. 7(a) and (b), as the thickness of the negative curvature tube increases, the resonance wavelength blueshifts and the loss accentuates. When the inner diameter is 3 μm or 4 μm, the temperature sensitivity is 14.4 nm/°C, but the resonance is stronger when $\boldsymbol{d_2} = 4.0$ μm. Hence, the optimal $\boldsymbol{d_2}$ is 4.0 μm. Consequently, the optimal parameters of the ARF-SPR temperature sensor are $\boldsymbol{D} = 18.0$ μm, $\boldsymbol{t} = 0$ 8 μm, C_2H_5OH: $CHCl_3 = 1{:}9$, $\boldsymbol{d_1} = 5.4$ μm, and $\boldsymbol{d_2} = 4.0$ μm.

After obtaining the most suitable structure parameters, the ARF can be fabricated industrially by tube stacking technology [34]. Firstly, three circular holes with different sizes are drilled into the center of the SiO_2 columnar glass by rotary sonic drilling [35] to manufacture the negative curvature tubes. The anti-resonance tubes with diameters of $\boldsymbol{d_1}$ and $\boldsymbol{d_2}$ are then combined into a conjoined tube, and six groups are produced by the same method. Finally, the conjoined tubes are uniformly arranged in the large glass tube with an inner radius of $\boldsymbol{R_1}$. The preform is produced and the optical fiber is drawn, and then cut off both ends of the ARF to obtain the structure of the middle part. Place the gold wire at the capillary port, use tungsten wire to push the gold wire into it, and melt it together [36]. Heat the splicing part to the melting point of the gold wire (approximately 1064 °C), and utilize high-pressure helium to push the liquid gold medium into the anti-resonance tube. Finally, using the method given in reference [37], a pulsed laser was used to drill holes on the side of the ARF and inject a temperature sensitive liquid. The process of temperature detection by the ARF-SPR sensor is shown in Fig. 8.

The SMF is connected to both ends of the sensor by an optical fiber fusion splicer, and connected to the light source and optical spectrum analyzer (OSA), respectively. The sensor is placed in the environment where the temperature is to be detected. The light source is turned on. The wave reaches the ARF-SPR sensor through the SMF and then the OSA through the SMF at the other end and is converted into an electrical signal. Finally, the electrical signal is recorded by a personal computer (PC) through a data line for analysis.

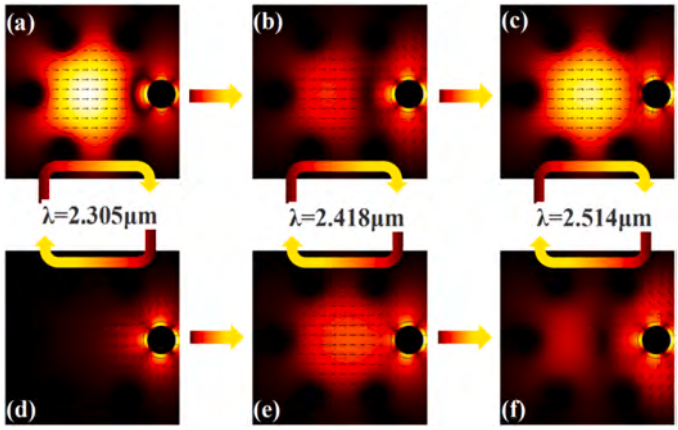

Fig. 10. Mode field distributions: (a)–(c) Fundamental mode and (d)–(f) Corresponding SPP mode at 2.305 μm, 2.418 μm, and 2.514 μm when $\boldsymbol{T} = 45\ ^{\circ}\mathrm{C}$.

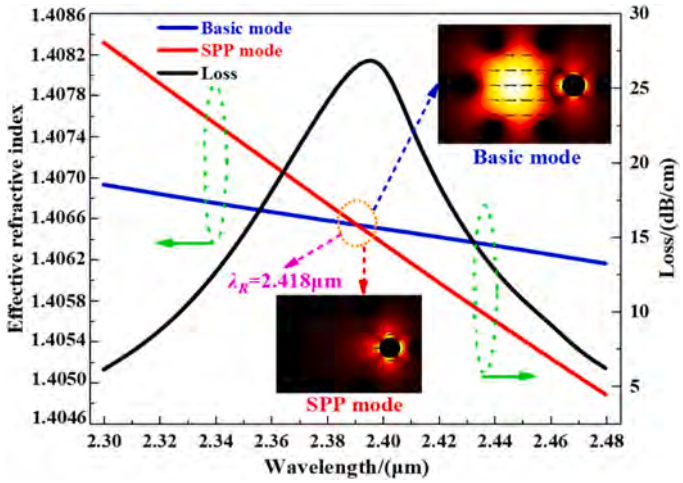

Fig. 11. Relationship between the real part of the refractive index of the basic and SPP modes; Loss of the fundamental mode and resonance wavelength for $\boldsymbol{T}$ being 45 °C.

After identifying the corresponding resonance wavelength, the temperature can be determined.

3. Results and discussion

3.1. Coupling properties

The properties of the ARF-SPR temperature sensor are mainly characterized by the loss spectrum of the fundamental mode in a certain band. The fundamental mode of ARF has two mutually orthogonal polarization directions, i.e. *x*-pol and *y*-pol. The electric field directions of the two polarizations are perpendicular to each other, and the sensing performance always shows a discrepancy. Hence, it is particularly momentous to select a reasonable polarization direction. Fig. 9 presents the loss spectra of the two polarizations at 45 °C and 50 °C together with the correlative mode field distributions. The *x*-pol has not only the perfect resonance peak and obvious resonance wavelength difference, but also the core with concentrated photon energy. There is no available formant in *y*-pol and there is leakage of guided mode energy. Hence, *x*-pol is selected in the performance analysis.

After ascertaining the polarization direction, the electric field distributions of the fundamental mode and SPP mode at the resonance wavelength and its vicinity are analyzed as shown in Fig. 10(a)–(f):

Fig. 10 (a)–(c) and (d)–(f) are the fundamental and corresponding SPP modes at the three wavelengths, respectively, and 2.418 μm is the resonance wavelength. Before reaching the resonance wavelength, the photon energy is mainly concentrated in the fundamental mode, while the energy in the proximity of the metal surface is less. With a redshift of the wavelength, the energy of the fundamental mode is gradually transferred to the SPP mode, so that the number of photons on the surface of the gold medium increases dramatically and reaches the resonance wavelength to excite SPR. When the resonance wavelength is exceeded, the energy is gradually transferred

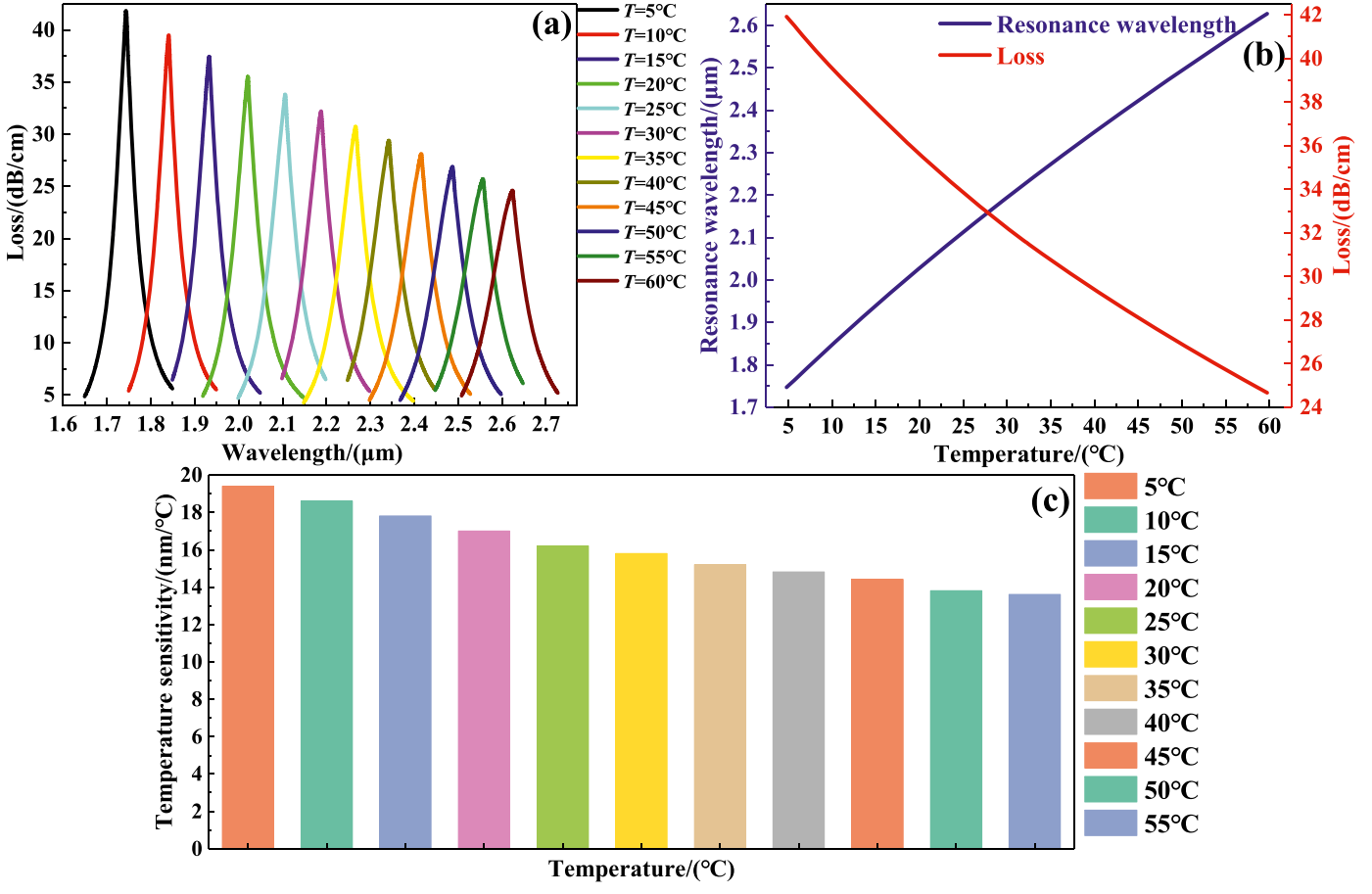

Fig. 12. (a) Loss spectra of the fundamental mode for T = 5–60 °C; (b) Resonance wavelength and loss peak at different temperatures, and (c) Temperature sensitivity.

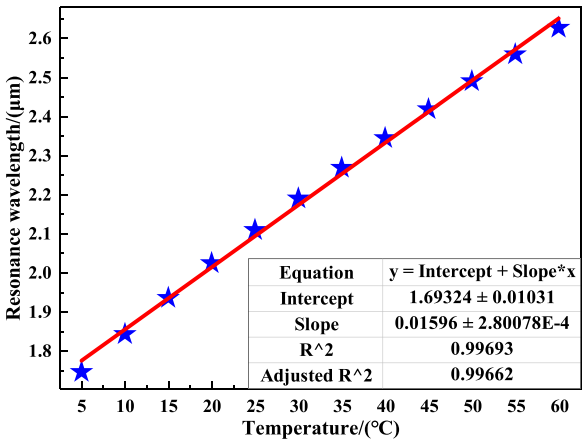

Fig. 13. Linear fitting of the resonance wavelength with respect to temperature.

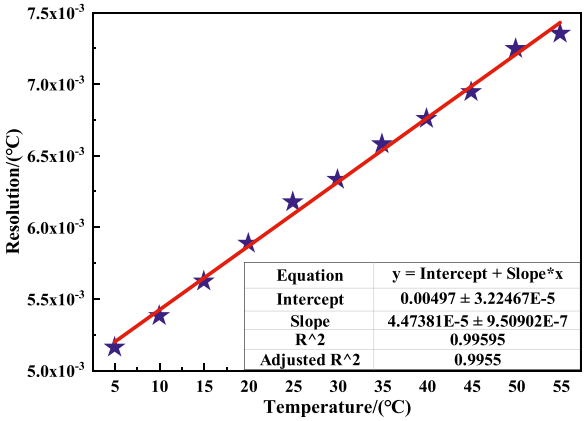

Fig. 14. Linear fitting of the resolution of the ARF-SPR temperature sensor.

to the core again. The principle of SPR can also be explained by the mode coupling properties shown in Fig. 11.

When $\lambda < 2.418$ μm, the real part of the effective refractive index of the SPP mode is larger than that of the fundamental mode. When $\lambda = 2.418$ μm, the fundamental mode energy is continuously absorbed by the SPW near the gold medium, so that the SPP mode energy increases. When $\lambda > 2.418$ μm, the real part of the refractive index of the fundamental mode is higher than that of the SPP mode. Before the resonance wavelength, a large number of electrons are attracted to the region of excess positive charge and neutralized due to the presence of Coulomb force, and resulting in ascending loss. When the Coulomb force and the repulsive force between electrons are balanced, the loss peak appears. If the wavelength is greater than the resonant wavelength, the repulsion between electrons adds sharply and drives electrons out of the region, thereby reducing losses. This is why the loss is first proportional to the wavelength and then inversely proportional.

3.2. *Temperature sensing*

Different temperatures result in different loss curves. As the temperature changes according to a certain law, the resonance wavelength of the loss spectrum also shifts red or blue according to the corresponding trend. The temperature sensitivity determined by Eq. 10 can be obtained by calculating the resonance wavelength difference of the loss function at adjacent temperatures. In addition, the loss curve of the ARF-SPR sensor in the temperature range of 5–60 °C is analyzed by COMSOL using the parameter scanning method as shown in Fig. 12(a). The resonance wavelength and temperature sensitivity are summarized in Fig. 12(b)–(c).

As expressed in Fig. 12, the ARF-SPR sensor can detect temperatures in the range of 5–60 °C. With the enlargement of wavelength, the loss of the basic mode at any temperature increases first and then decreases. When the temperature rises continuously, the resonance wavelength moves to the long wavelength direction, and the height of the loss peak descends incessantly. The minimum loss is 24.603 dB/cm at 60 °C, which is conducive to long-distance detection. Moreover, the temperature sensitivity of the ARF-SPR sensor is inversely proportional to the temperature and is all above 13.6 nm/°C. When $\boldsymbol{t} = 5$ °C, the temperature sensitivity of the sensor shows the maximum value (19.4 nm/°C) and the average temperature sensitivity is as high as 16.055 nm/°C, which is higher than

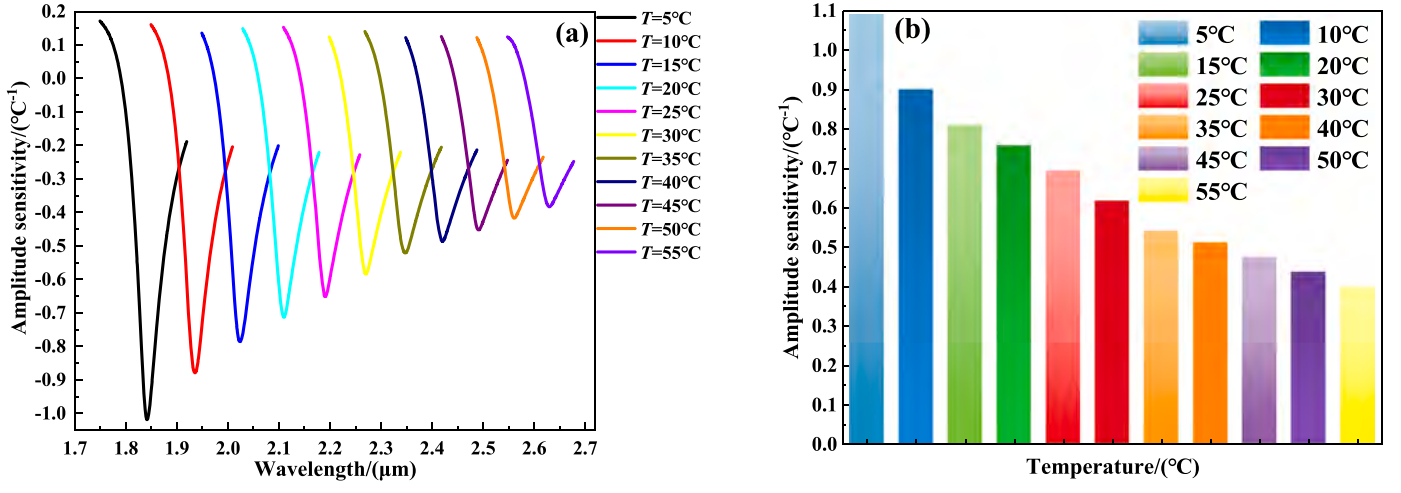

Fig. 15. (a) Amplitude sensitivity curves and (b) Summary of the maximum amplitude sensitivity from 5 °C to 55 °C.

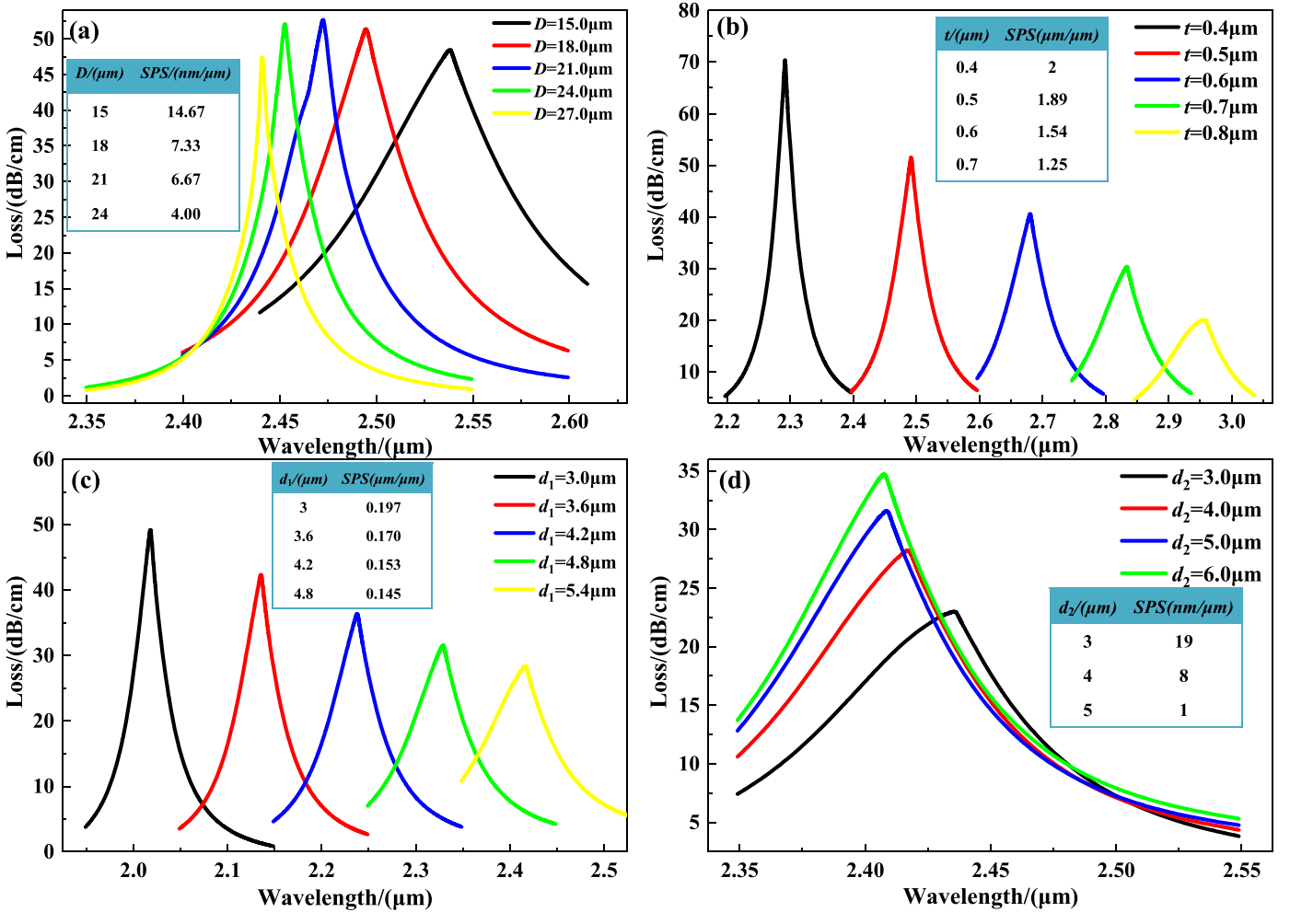

Fig. 16. Structural parameter sensitivity: (a) Core diameter, (b) Thickness of the negative curvature tube, (c) Inner diameter of the inner tube, and (d) Inner diameter of the outer tube at 45 °C.

described in Refs. [23,24]. We derive the relationship between the resonance wavelength of the ARF-SPR sensor and the temperature by linear fitting as shown by Eq. (11):

$$\lambda_R = 1.693 + 0.016T, (5°C < T < 60°C), \tag{11}$$

where $\boldsymbol{\lambda_R}$ is the resonance wavelength and T is the temperature. The fit in Fig. 13 shows excellent linearity with an adjusted R^2 of 99.66 %.

The resolution that is inversely proportional to the temperature sensitivity refers to the ability of the sensor to detect the smallest change. If the resolution of the ARF-SPR sensor is poor, it cannot sense small temperature changes in the environment and produce big errors under certain circumstances. The resolution of the ARF-SPR temperature sensor is described by Eq. (12) [38]:

$$R_n = \frac{\Delta n_a \Delta\lambda_{\min}}{\Delta\lambda_{peak}} = \frac{\Delta\lambda_{\min}}{S_n}, \tag{12}$$

where S_n is the temperature sensitivity and $\triangle\lambda_{min}$ is the minimum measured value of OSA, which is generally related to the instrument. Under these conditions, $\triangle\lambda_{min} = 0.1$ nm. In the same way, the resolution of the ARF-SPR sensor is linearly fitted by Eq. (13). Fig. 14 indicates that the linearity is also excellent with an adjusted R^2 of 99.55 %. The resolution is proportional to the temperature, and the optimal resolution is 5.15×10^{-3} °C.

$$R_n = 4.97 \times 10^{-2} + 4.47 \times 10^{-5}T, \left(5°C < T < 55°C\right), \tag{13}$$

3.3. Amplitude sensitivity

Although wavelength interrogation is widely used in SPR sensors, the spectra need to be operated to measure the sensitivity making the process quite complex. In engineering, there is also a sensitivity measurement method with a lower cost and simpler operation by observing the change of the optical power transmitted at different temperatures at certain wavelengths. This is called the amplitude sensitivity and is obtained by Eq. (14) [27]:

$$S_A = -\frac{1}{\alpha(\lambda, T)} \frac{\partial\alpha(\lambda, T)}{\partial T}, \tag{14}$$

where $\alpha(\lambda, T)$ is the loss at a specific wavelength and $\partial\alpha(\lambda, T)$ and ∂T are the differences in the loss and temperature, respectively. Fig. 15(a) and (b) present the amplitude sensitivity function of the ARF-SPR temperature sensor and summarize the maximum amplitude sensitivity at each temperature.

For the amplitude sensitivity curve at a certain temperature, the variation trend with wavelength first increases and then decreases. With increasing temperature, the amplitude sensitivity curve gradually moves to the long wavelength direction, and the maximum amplitude sensitivity gradually falls. In addition, the maximum amplitude sensitivity at all temperatures is above 0.398 °C^{-1}, and the maximum amplitude sensitivity of the temperature sensor is 1.089 °C^{-1} when $\boldsymbol{T} = 5$ °C.

3.4. Structural parameter sensitivity

In the manufacturing process of ARF, the size of ARF may not reach the predetermined value because of temperature, stress, and other factors, which may compromise the performance of the sensor. If a small size change results in a great discrepancy in performance, the ARF sensor is less practical. The structural parameter sensitivity is defined as the ratio of the change of the resonance wavelength to the change of structural parameters and can be utilized to evaluate the stability of ARF-SPR. Fig. 16(a)–(d) show the structural parameter sensitivity of the core diameter, the thickness of the negative curvature tube, as well as the inner diameter of the inner tube and inner diameter of the outer tube at 45 °C.

It is obvious that as the four structural sizes increase, the sensitivity of the corresponding structural parameters decreases. Therefore, it is necessary to select a larger size as much as possible in order to meet the design requirements when preparing the ARF. The resonance wavelength blueshifts when $\boldsymbol{D}$ and $\boldsymbol{d_2}$ go up, and the resonance wavelength redshifts when $\boldsymbol{t}$ and $\boldsymbol{d_1}$ increase. In addition, the minimum sensitivity of the four structural parameters is 4.00 nm/μm, 1.25 μm/μm, 0.145 μm/μm, 1 nm/μm, which is far lower than those reported in Ref. [20]. Consequently, the ARF-SPR sensor has a large tolerance and good practicability.

3.5. Detection distance

In actual applications, the detected environment is sometimes complex. If manual detection is carried out, the sensor may have to operate from a long detection distance. The propagation speed of the x and y polarization of the fundamental mode in the ARF is different. If the distance between the two polarizations is too large in the transmission process, the basic mode will be distorted and cannot be detected. The detection distance of the sensor can be measured by Eq. (15) [39]:

$$L = \frac{c \times 10ps}{n_{eff}^{even} - n_{eff}^{odd}} = \frac{3 \times 10^{-3}}{n_{eff}^{even} - n_{eff}^{odd}}(m), \tag{15}$$

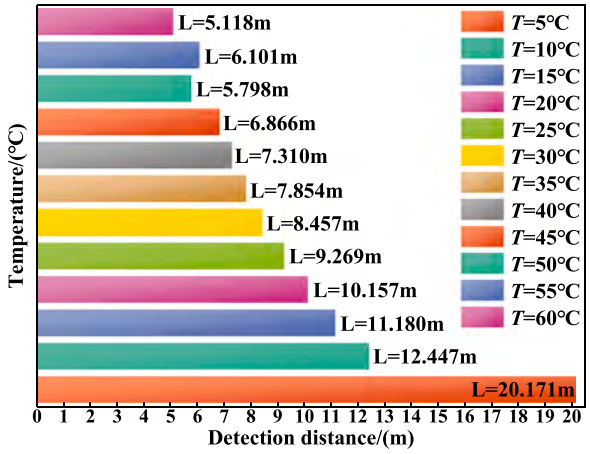

Fig. 17. Detection distance of the ARF-SPR sensor.

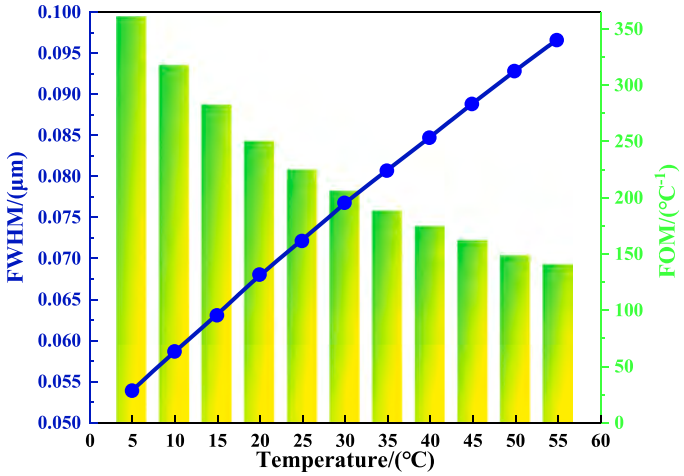

Fig. 18. FOM of the ARF-SPR temperature sensor in 5–55 °C.

where c is the speed of light, and n_{eff}^{even} and n_{eff}^{odd} are the effective refractive indexes of the x-pol and y-pol of basic modes, respectively. Fig. 17 plots the detection distance of the ARF-SPR sensor at different ambient temperatures. All the detection distance is negatively correlated with the temperature and is above 5.11 m. In addition, the maximum detection distance of the sensor is 20.171 m when the temperature is 5 °C, which is sufficient for most applications.

3.6. Figure of merit (FOM)

The overall performance of the ARF-SPR temperature sensor can be analyzed by the FOM (Figure of merit) expressed in Eq. (16) [40], It is in fact one of the important performance parameters of optical fiber sensors.

$$FOM = \frac{S_n}{FWHM}, \tag{16}$$

where S_n is the temperature sensitivity and FWHM is the corresponding full-width at half-maximum of the loss peak. Fig. 18 indicates that the FOM declines with increasing temperature and it is inversely proportional to the FWHM. The FOM at any temperature is higher than 140.79 °C^{-1} and the maximum is 360.80 °C^{-1} at 5 °C, which is better than those described in Ref. [41].

3.7. Performance comparison

To illustrate the advantages of our ARF-SPR temperature sensor, the plasmonic materials, temperature range, temperature sensitivity, amplitude sensitivity, FOM, and other characteristics are compared to those of sensors reported recently as shown in Table 1.

Table 1
Comparison of sensing properties.

Ref	Fiber structure	Metal	Temperature sensitivity	Thermosensitive Liquid	Resolution	FOM
[42]	Hexagonal honeycomb PCF	Au	0.72 nm/°C	–	–	–
[43]	6 liquid holes PCF	Au	3.08 nm/°C	C_2H_5OH	1.33×10^{-2} °C	121.22 $°C^{-1}$
[23]	Conjoined tubular ARF	Au	3.60 nm/°C	C_2H_5OH	–	–
[24]	6 negative curvature tube ARF	Au	5.05 nm/°C	C_2H_5OH and $CHCl_3$	1.56×10^{-2} °C	22.52 $°C^{-1}$
[44]	Dual channel PCF	Au	2.36 nm/°C	PDMS	–	–
Ours	***Conjoined-tube ARF***	***Au***	***19.40 nm/°C***	***C_2H_5OH and $CHCl_3$***	*5.15×10^{-3} °C*	***360.80 $°C^{-1}$***

Compared with other optical fiber temperature sensors proposed recently, our ARF-SPR has a simpler structure and higher resolution. Furthermore, the temperature sensitivity and FOM are much higher than those of other sensors, making it suitable for environmental monitoring with high accuracy.

4. Conclusion

An ARF-SPR temperature sensor composed of six conjoined negative curvature anti-resonance tubes is designed and the structural parameters are optimized systematically. The core of the sensor is filled with a thermosensitive liquid of C_2H_5OH: $CHCl_3 = 1$: 9. The numerical results illustrate that the ARF-SPR temperature sensor can detect the ambient temperature in the range of 5–55 °C, and the maximum temperature sensitivity and amplitude sensitivity are 19.40 nm/°C and 1.089 $°C^{-1}$ at 5 °C, respectively. The minimum temperature change detected by the sensor is 5.15×10^{-3} °C and the maximum detection distance is 20.17 m, making the sensor suitable for real-time environmental monitoring, military and industrial applications, as well as biological research.

Declaration of Competing Interest

There is no conflict of interest between all authors.

Data Availability

The authors do not have permission to share data.

Acknowledgments

This work was jointly supported by National Natural Science Foundation of China [grant number 12174022], Beijing Municipal Natural Science Foundation [grant number 1232028], City University of Hong Kong Strategic Research Grant (SRG) [grant number 7005505], and City University of Hong Kong Donation Research Grant [grant number DON-RMG No. 9229021].

References

[1] T.G. Giallorenzi, J.A. Bucaro, A. Dandridge, et al., Optical fiber sensor technology, IEEE Trans. Microw. Theory Tech. 30 (1982) 472–511.
[2] X. Zhang, X. Zhou, S. Wang, et al., High-sensitivity fiber-optic Fabry-Perot transverse load sensor based on bubble microcavity, Sens. Actuators A: Phys. 335 (2022), 113375.
[3] J. Chen, B. Liu, H. Zhang, Review of fiber Bragg grating sensor technology, Front. Optoelectron. China 4 (2011) 204–212.
[4] M. Kanso, S. Cuenot, G. Louarn, Sensitivity of optical fiber sensor based on surface plasmon resonance: modeling and experiments, Plasmonics 3 (2008) 49–57.
[5] R.C. Jorgenson, S.S. Yee, A fiber-optic chemical sensor based on surface plasmon resonance, Sens. Actuators B: Chem. 12 (1993) 213–220.
[6] H.Y. Lin, C.H. Huang, G.L. Cheng, et al., Tapered optical fiber sensor based on localized surface plasmon resonance, Opt. Express 20 (2012) 21693–21701.
[7] R.H. Renard, Total reflection: a new evaluation of the Goos–Hänchen shift, JOSA 54 (1964) 1190–1197.
[8] P.A. Van Der Merwe, Surface plasmon resonance, Protein-Ligand Interact.: Hydrodyn. Calorim. 1 (2001) 137–170.
[9] J. Homola, Surface plasmon resonance sensors for detection of chemical and biological species, Chem. Rev. 108 (2008) 462–493.
[10] Y. Chen, H. Ming, Review of surface plasmon resonance and localized surface plasmon resonance sensor, Photon. Sens. 2 (2012) 37–49.
[11] R. Slavík, J. Homola, J. Čtyroký, Single-mode optical fiber surface plasmon resonance sensor, Sens. Actuators B: Chem. 54 (1999) 74–79.
[12] E. Liu, S. Liang, J. Liu, Double-cladding structure dependence of guiding characteristics in six-fold symmetric photonic quasi-crystal fiber, Superlattices Microstruct. 130 (2019) 61–67.
[13] E. Liu, W. Tan, B. Yan, J. Xie, R. Ge, J. Liu, Robust transmission of orbital angular momentum mode based on a dual-cladding photonic quasi-crystal fiber, J. Phys. D: Appl. Phys. 52 (2019), 325110.
[14] J.N. Dash, R. Jha, Graphene-Based Birefringent photonic crystal fiber sensor using surface plasmon resonance, IEEE Photonics Technol. Lett. 26 (2014) 1092–1095.
[15] S.I. Azzam, M.F.O. Hameed, R.E.A. Shehata, et al., Multichannel photonic crystal fiber surface plasmon resonance based sensor, Opt. Quantum Electron. 48 (2016) 1–11.
[16] T. Guo, Fiber grating-assisted surface plasmon resonance for biochemical and electrochemical sensing, J. Light. Technol. 35 (2017) 3323–3333.
[17] A.K. Sharma, B.D. Gupta, Theoretical model of a fiber optic remote sensor based on surface plasmon resonance for temperature detection, Opt. Fiber Technol. 12 (2006) 87–100.
[18] J.N. Dash, R. Jha, Graphene-based birefringent photonic crystal fiber sensor using surface plasmon resonance, IEEE Photonics Technol. Lett. 26 (2014) 1092–1095.
[19] X. Guo, L. Han, F. Liu, et al., Refractive index sensing characteristics of dual-core PCF based on surface plasmon resonance, Optik 218 (2020), 164796.
[20] E. Liu, B. Yan, H. Zhou, et al., OAM mode-excited surface plasmon resonance for refractive index sensing based on a photonic quasi-crystal fiber, JOSA B 38 (2021). F16-F22.

[21] W. Zhang, Z. Lian, T. Benson, et al., Theoretical demonstration of single polarization single mode hollow core anti-resonance fiber using surface plasmon resonance, J. Opt. 21 (2019), 025001.
[22] J. Lv, H. Fu, C. Hu, et al., Double-formant surface plasmon resonance for refractive index sensing by anti-resonance fibers with high sensitivity and wide detection range, Results Phys. 40 (2022), 105876.
[23] Q. Wang, X. Zhang, X. Yan, et al., Design of a surface plasmon resonance temperature sensor with multi-wavebands based on conjoined-tubular anti-resonance fiber, Photonics 8 (2021) 231.
[24] Q. Chen, H. Chen, Y. Liu, et al., A self-verification temperature sensor based on surface plasmon resonance in a hollow core negative curvature fiber, J. Phys. D: Appl. Phys. 55 (2022), 225208.
[25] X. Wang, J. Zhang, J. Zhu, et al., Refractive index sensing of double Fano resonance excited by nano-cube array coupled with multilayer all-dielectric film, Chin. Phys. B 31 (2021), 024210.
[26] J.K. Zhu, X.X. Wang, Y.P. Qi, et al., Self-reference plasmonic sensor based on functional layer film composed of Au/Si gratings, Chin. Phys. B 31 (2022), 014206.
[27] C. Liu, H. Fu, Y. Lv, et al., $HE_{1,1}$ mode-excited surface plasmon resonance for refractive index sensing by photonic crystal fibers with high sensitivity and long detection distance, Optik 265 (2022), 169471.
[28] C. Liu, J. Lü, W. Liu, et al., Overview of refractive index sensors comprising photonic crystal fibers based on the surface plasmon resonance effect, Chin. Opt. Lett. 19 (2021), 102202.
[29] H. Fu, C. Liu, C. Hu, et al., Circular photonic crystal fiber supporting 118 orbital angular momentum modes transmission, Opt. Eng. 60 (2021), 076102.
[30] G. Ghosh, M. Endo, T. Iwasaki, Temperature-dependent Sellmeier coefficients and chromatic dispersions for some optical fiber glasses, J. Light. Technol. 12 (1994) 1338–1342.
[31] S. Kedenburg, M. Vieweg, T. Gissibl, et al., Linear refractive index and absorption measurements of nonlinear optical liquids in the visible and near-infrared spectral region, Opt. Mater. Express 2 (2012) 1588–1611.
[32] E. Kretschmann, H. Raether, Radiative decay of non radiative surface plasmons excited by light, Z. für Naturforsch. A 23 (1968) 2135–2136.
[33] A.A. Rifat, G.A. Mahdiraji, D.M. Chow, et al., Photonic crystal fiber-based surface plasmon resonance sensor with selective analyte channels and graphene-silver deposited core, Sensors 15 (2015) 11499–11510.
[34] H. Fu, Z. Yi, Y. Shi, et al., Circular anti-resonance fibre supporting orbital angular momentum modes with flat dispersion, high purity and low confinement loss, J. Mod. Opt. 68 (2021) 784–791.
[35] H. Fu, M. Zhu, C. Liu, et al., Photonic crystal fiber supporting 394 orbital angular momentum modes with flat dispersion, low nonlinear coefficient, and high mode quality, Opt. Eng. 61 (2022), 026111.
[36] H.K. Tyagi, H.W. Lee, P. Uebel, M.A. Schmidt, N. Joly, M. Scharrer, P.S.J. Russell, Plasmon resonances on gold nanowires directly drawn in a step-index fiber, Opt. Lett. 35 (2010) 2573–2575.
[37] J.P. Parry, B.C. Griffiths, N. Gayraud, et al., Towards practical gas sensing with micro-structured fibers, Meas. Sci. Technol. 20 (2009), 075301.
[38] B.H. Almewafy, N.F.F. Areed, M.F.O. Hameed, et al., Modified D-shaped SPR PCF polarization filter at telecommunication wavelengths, Opt. Quantum Electron. 51 (2019) 1–14.
[39] C. Liu, H. Fu, C. Hu, et al., Optimization of photonic crystal fibers for transmission of orbital angular momentum modes, Opt. Quantum Electron. 53 (1) (2021) 18.
[40] A.K. Mishra, S.K. Mishra, B.D. Gupta, SPR based fiber optic sensor for refractive index sensing with enhanced detection accuracy and figure of merit in visible region, Opt. Commun. 344 (2015) 86–91.
[41] N. Luan, J. Yao, Refractive index and temperature sensing based on surface plasmon resonance and directional resonance coupling in a PCF, IEEE Photonics J. 9 (2017) 1–7.
[42] Y. Peng, J. Hou, Z. Huang, et al., Temperature sensor based on surface plasmon resonance within selectively coated photonic crystal fiber, Appl. Opt. 51 (2012) 6361–6367.
[43] C. Liu, F. Wang, J. Lv, et al., A highly temperature-sensitive photonic crystal fiber based on surface plasmon resonance, Opt. Commun. 359 (2016) 378–382.
[44] D. Wang, Z. Yi, G. Ma, et al., Two-channel photonic crystal fiber based on surface plasmon resonance for magnetic field and temperature dual-parameter sensing, Phys. Chem. Chem. Phys. 24 (2022) 21233–21241.